

ELM triggering conditions for the integrated modeling of H-mode plasmas *)

A.Y. PANKIN **)

SAIC, 10260 Campus Point Dr., San Diego, CA 92121, USA

G. BATEMAN

Lehigh University, Bethlehem, PA 18015, USA

D.P. BRENNAN

MIT, Cambridge, MA 02139, USA

D.D. SCHNACK

SAIC, 10260 Campus Point Dr., San Diego, CA 92121, USA

P.B. SNYDER

General Atomics, San Diego, CA 92186, USA

I. VOITSEKHOVITCH

JET-UKAEA, Culham Science Centre, UK

A.H. KRITZ

Lehigh University, Bethlehem, PA 18015, USA

S. KRUGER

Tech-X, Boulder, CO 80303, USA

G. JANESCHITZ

FZK-PL-Fusion, Karlsruhe, Germany

T. ONJUN

Sirindhorn Internat. Inst. of Technology, Klong Luang, Pathumthani 12121, Thailand

G.W. PACHER

Hydro-Québec, Varennes, Québec, Canada

H.D. PACHER

INRS, Québec, Canada

Received 31 January 2005

Recent advances in the integrated modeling of ELMy H-mode plasmas are presented. A new model for the H-mode pedestal and for the triggering of ELMs predicts the height, width, and shape of the H-mode pedestal and the frequency and width of ELMs. The model for the pedestal and ELMs is used in the ASTRA integrated transport code to follow the time evolution of tokamak discharges from L-mode through the transition from L-mode to H-mode, with the formation of the H-mode pedestal, and, subsequently, to the triggering of ELMs. Turbulence driven by the ion temperature gradient mode, resistive ballooning mode, trapped electron mode, and electron temperature gradient mode contributes to the anomalous thermal transport at the plasma edge in this model. Formation of the pedestal and the L-H transition is the direct result of $\vec{E}_r \times \vec{B}$ flow shear suppression

*) Presented at the Workshop "Electric Fields Structures and Relaxation in Edge Plasmas", Nice, France, October 26–27, 2004.

**) E-mail: alexei.y.pankin@saic.com

of anomalous transport. The periodic ELM crashes are triggered by MHD instabilities. Two mechanisms for triggering ELMs are considered: ELMs are triggered by ballooning modes if the pressure gradient exceeds the ballooning threshold or by peeling modes if the edge current density exceeds the peeling mode threshold. The BALOO, DCON, and ELITE ideal MHD stability codes are used to derive a new parametric expression for the peeling-ballooning threshold. The new dependence for the peeling-ballooning threshold is implemented in the ASTRA transport code. Results of integrated modeling of DIII-D like discharges are presented and compared with experimental observations. The results from the ideal MHD stability codes are compared with results from the resistive MHD stability code NIMROD.

PACS: ???

Key words: ???

I Introduction

Integrated modeling of the core of tokamak plasmas has been developed for decades. An impressive agreement with experimental observations has been achieved with different transport models such as the Multi-Mode (MM), GLF23, and mixed Bohm/gyro-Bohm (or JET) transport models. Transport modeling of the edge of tokamak plasmas is another challenging problem. A wide range of time and length scales need to be considered and many different elements of physics are involved at the plasma edge. The physics topics that are critically important for the plasma edge are the transition from low- to high- confinement regime (L-H transition), H-mode pedestal build up, anomalous and neoclassical transport at the plasma edge, role of the $\vec{E}_r \times \vec{B}$ flow shear, triggering and dynamics of the edge localized modes (ELMs). None of these problems is completely understood. Numerous theories, hypothesis, and ideas are being considered for each of these problems. One of the effective ways to test ideas for physics models is to combine them within an integrative modeling code and compare the simulation results with the experiments. Integrated modeling studies that self-consistently take into account the effects of the plasma edge have been developing during the last decade [1–5]. Some of these simulations are rather comprehensive and take into account MHD equilibrium, turbulent anomalous radial transport, neutral gas transport, atomic and molecular physics, and plasma-wall interactions.

A model for the H-mode pedestal has been recently developed by Zolotukhin *et al.* [6] and Pacher *et al.* [1]. The model takes into account the stabilizing effects of the $\vec{E}_r \times \vec{B}$ flow shear and large magnetic shear at the plasma edge. While the stabilizing effect of the $\vec{E}_r \times \vec{B}$ flow shear is well recognized [7–10], the stabilizing effect of the large magnetic shear is not so well known. The stabilizing effect of large magnetic shear is at the opposite extreme of the stabilizing effect resulting from small magnetic shear in the neighborhood of internal transport barriers (ITBs). Nevertheless, the ITB turbulence suppression for large magnetic shear has been demonstrated in rtheory [11], in gyro-kinetic turbulence simulations [12], and in some transport simulations [13]. In addition, the stabilizing effect of large magnetic

shear can be included to reproduce the effect of ELMs on the H-mode pedestal [14]. After taking into account of the effects of $\vec{E}_r \times \vec{B}$ flow shear and large magnetic shear, the resulting effective thermal diffusivity has the form:

$$\chi_{\text{eff}} = \chi_{\text{anom}} F_s + \chi_{\text{neoc1}}, \quad (1)$$

where χ_{anom} is the anomalous thermal diffusivity from the transport model, χ_{neoc1} is the neoclassical thermal diffusivity,

$$F_s = \frac{\mathcal{G}(s)}{1 + \left(\frac{\omega_{E \times B}}{\hat{\gamma}_{\text{ITG}}} \right)^2}, \quad (2)$$

$\mathcal{G}(s)$ is the magnetic shear stabilization function, $\omega_{E \times B}$ is the $\vec{E}_r \times \vec{B}$ flow shearing rate, and $\hat{\gamma}_{\text{ITG}}$ is the volume average of ITG growth rate, without stabilization, inside 0.9 of the minor radius. The magnetic shear stabilization function used by Zolotukhin *et al.* [6] has the form $\mathcal{G}(s) = s^{-1.8}$. An additional threshold dependence has been introduced by Pacher *et al.* [1] into the magnetic shear stabilization function $\mathcal{G}(s) = \min(1, (s - s_{\text{th}})^{-2})$.

A new model for the H-mode pedestal and ELMs has been recently developed by Pankin *et al* [5]. The model predicts the height, width, and shape of the H-mode pedestal as well as the frequency and width of ELMs. The model for the H-mode pedestal in tokamak plasmas is based on flow shear reduction of anomalous transport. The formation of the pedestal and the L-H transition in this model are the direct result of $\vec{E}_r \times \vec{B}$ flow shear suppression of transport. The magnetic shear factor $\mathcal{G}(s)$ is not part of the model since the magnetic shear stabilization effect is already included in the transport model, as it is in the Weiland model used in that study [15].

Edge localized modes (ELMs) are among the determinant factors at the plasma edge that affect the whole plasma profiles, since up to 10% of the plasma energy can be removed by a single ELM crash. An ELM crash can be initiated either by a pressure driven ballooning instability or by a current driven peeling instability [16, 17]. Two mechanisms for triggering ELMs have been considered in the model for ELMs [5]. ELMs are triggered by ballooning modes if the pressure gradient exceeds the ballooning limit or by peeling modes if the edge current density exceeds the peeling mode criterion. The model for the pedestal and ELMs has been used in a predictive integrated modeling code to follow the time evolution of tokamak discharges from L-mode through the transition from L-mode to H-mode, with the formation of the H-mode pedestal, and, subsequently, the triggering of ELMs.

The model for the H-mode pedestal and ELMs [5] is advanced in this paper. The ELM triggering conditions are studied with the MHD stability codes BALOO [18], DCON [19], and ELITE [20]. These MHD instability codes are used to compute the combined peeling-ballooning threshold, which are then used to derive fitting expressions that are included in the model. Using these MHD instability enhances the model and extends the level of its applicability. In particular, the ballooning criterion implemented previously is valid only in the first ballooning stability limit,

while many recent DIII-D discharges operate in the second stability domain. The improved stability criterion model is tested in the integrated modeling code AS-TRA [21]. Cases with low and high triangularity are considered.

This paper is organized in the following manner. In Section II, a model for the H-mode pedestal and ELMs is introduced. The model is based on $\vec{E}_r \times \vec{B}$ flow shear suppression of anomalous thermal transport. Two ELM triggering mechanisms are considered: ELM crashes are caused either by ballooning mode instabilities or by peeling mode instabilities. Section III contains an MHD stability analysis of two cases, which are based on DIII-D equilibria with high and low triangularity. The TOQ code is used to generate the equilibria, and the BALOO, DCON, and ELITE codes are used to study the MHD stability at the plasma edge. The pedestal temperature, plasma density, and bootstrap current are varied in a systematic manner to find a peeling-ballooning threshold. Fitting expressions for the threshold is implemented in the model for the H-mode pedestal and ELMs. The details of implementation and simulation results are reported in Section IV. Discussion of the results and conclusions are presented in the Section V.

II Combined model for H-mode pedestal and ELM crashes

The model used in this paper for the H-mode pedestal and ELMs has been introduced in Ref. [5]. The H-mode pedestal formation is computed by suppression of the anomalous transport at the plasma edge. In order to take into account the fact that different instabilities are suppressed by the $\vec{E}_r \times \vec{B}$ flow shear at different rates, separate flow shear suppression functions $F_l^{(j)}$ are used. The contributions from the different instabilities together with the neoclassical thermal diffusivity, χ_{neo} , constitute the total ion and electron thermal diffusivity:

$$\chi_i = F_{\text{TGM}}^{(i)} \chi_{\text{TGM}}^{(i)} + F_{\text{RB}}^{(i)} \chi_{\text{RB}}^{(i)} + \chi_{\text{neo}}^{(i)} \quad (3)$$

$$\chi_e = F_{\text{TGM}}^{(e)} \chi_{\text{TGM}}^{(e)} + F_{\text{RB}}^{(e)} \chi_{\text{RB}}^{(e)} + \chi_{\text{ETG}} + \chi_{\text{neo}}^{(e)}, \quad (4)$$

where

$$F_l^{(j)} = \frac{1}{1 + \alpha_l^{(j)} (\omega_{E \times B} \tau_{lj})^2}, \quad l = (\text{TGM}, \text{RB}), \quad j = (\text{ions}, \text{electrons}), \quad (5)$$

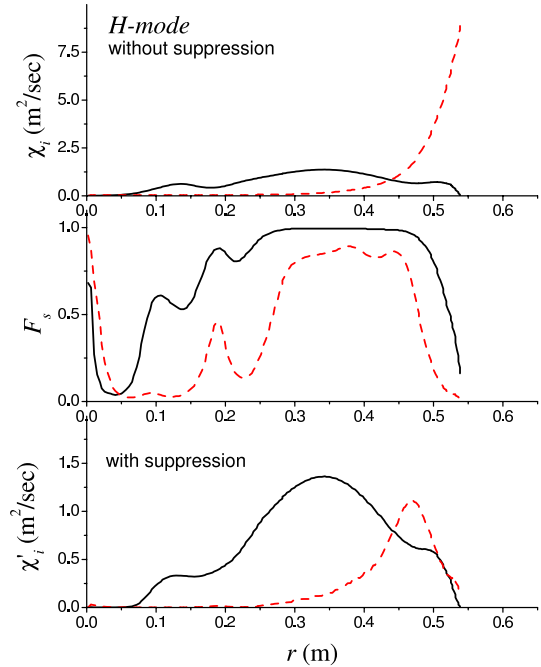
and $\chi_l^{(j)}$ is the anomalous thermal diffusivity without flow shear stabilization; τ_{lj} is the turbulence correlation time, which is estimated as $\tau_{lj} = L_l^2 / \chi_l^{(j)}$, where L_l is described below. The ITG and TEM thermal diffusivities, $\chi_{\text{TGM}}^{(j)}$, which are referred to as drift Temperature Gradient driven Modes (TGM) in this paper, are computed with the Weiland model [22], and the resistive ballooning diffusivities, $\chi_{\text{RB}}^{(j)}$, are computed with the Guzdar–Drake model [23]. The Weiland and Guzdar–Drake models are parts of the Multi-Mode (MM) transport model [15]. The ETG modes are not suppressed by the $\vec{E}_r \times \vec{B}$ flow shear. The ETG contribution, χ_{ETG} , is computed with the Horton model [24]. Neoclassical thermal contributions, χ_{neo} , are not affected by the $\vec{E}_r \times \vec{B}$ flow shear and are computed using the NCLASS

module [25]. For the TGM modes, L_{TGM} is set equal to the gyro-radius ρ_s , and for the resistive ballooning modes, L_{RB} is defined as [26]

$$L_{\text{RB}} = 2\pi q(a)R \left(\frac{2ne^2\eta_{\parallel}\rho_s}{m_e\Omega_e\sqrt{2RL_n}} \right)^{1/2}, \quad (6)$$

where $q(a)$ is the safety factor at the plasma edge, η_{\parallel} is the classical resistivity, Ω_e is the electron gyro-frequency, and $L_n = -dr/d\ln n$ is the scale length of the density gradient. The effect of the $\vec{E}_r \times \vec{B}$ flow shear is demonstrated in Fig. II.

Fig. 1. Radial profiles of ITG (solid curve) and resistive ballooning (dashed curve) ion thermal diffusivities without flow shear suppression (top panel); shear suppression functions for ITG (solid curve) and resistive ballooning (dashed curve) thermal transport (middle panel); and resulting thermal diffusivities after including the $\vec{E}_r \times \vec{B}$ flow shear suppression (bottom panel).



The flow shear rate $\omega_{E \times B}$ is defined as

$$\omega_{E \times B} \equiv \left| \frac{RB_{\theta}}{B_{\phi}} \frac{\partial}{\partial r} \left(\frac{E_r}{RB_{\theta}} \right) \right|, \quad (7)$$

where B_{θ} and B_{ϕ} are poloidal and toroidal components of the magnetic field; R is the major radius; and E_r is the radial component of electric field, which is computed from the first order radial force balance equation:

$$E_r = \frac{1}{Z_i e n_i} \frac{\partial p_i}{\partial r} - v_{\theta} B_{\phi} + v_{\phi} B_{\theta}, \quad (8)$$

where v_{θ} and v_{ϕ} are the poloidal and toroidal velocities respectively. The neoclassical expression for the poloidal rotation velocity in collisionless regime is used [27]:

$$v_{\theta} = \frac{0.8839 f_c}{e Z_i (0.3477 + 0.4058 f_c)} \frac{B_{\phi}}{B^2} \frac{\partial T_i}{\partial r}, \quad (9)$$

where $f_c = 1 - 1.46\epsilon^{1/2} + 0.46\epsilon^{3/2}$ is the average fraction of circulating particles and $\epsilon = r/R$ is the aspect ratio. The toroidal rotation velocity, v_ϕ is taken from the experimental data.

This part of the model is used to compute the H-mode pedestal formation. It remains unchanged relative to the model introduced in Ref. [5] except for an updated version of the model for neoclassical transport NCLASS and re-calibrated coefficients for the $\vec{E}_r \times \vec{B}$ flow shear suppression, $\alpha_l^{(j)}$. The remainder of the edge model is used to compute the trigger for ELM crashes and the consequences of each ELM crash.

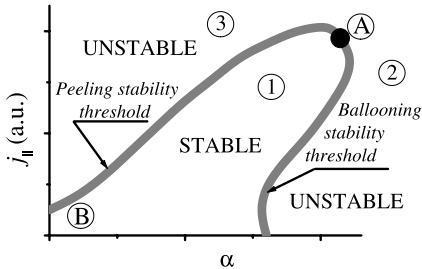


Fig. 2. Schematic diagram of an ELM crash. The stable region separates two unstable regions and . In the region , the ELM crashes are caused by the ballooning instability; in the region , the ELM crashes are caused by the peeling instability. The ballooning-peeling threshold is shown as a function of the parallel component of current density, $j_{||}$, and the normalized pressure gradient, α . In general, the parallel

component of plasma density destabilizes both the ballooning and peeling modes, and the pressure gradient stabilizes the peeling mode and destabilizes the ballooning mode.

An ELM crash in this model can be triggered either by a pressure driven ballooning instability or by a current driven peeling instability [16, 17]. The combined effects of ballooning and peeling criteria are shown on a schematic diagram in Fig. II [16, 28]. The part of the curve to the left of point A in Fig. II represents the peeling mode stability criterion; the part of the curve to the right of point A represents the ballooning mode stability criterion. A simplified condition for the peeling and ballooning threshold has been used in the previous version of the edge model [5]. In particular, the peeling criterion has been defined by an approximate analytical expression given in Ref. [29]. The peeling mode criterion involves the Mercier coefficient, which is proportional to the pressure gradient, and the parallel component of the plasma density. It reflects the fact that the peeling mode is destabilized by the parallel current and is stabilized by the plasma pressure gradient. This criterion for the peeling instability does not include a dependence on plasma shaping and does not account for the stabilizing effects of the vacuum region, except through an adjustable coefficient. The ballooning instability criterion used in the previous implementation of the model is valid only in the first ballooning stability limit. These limitations for the peeling and ballooning criteria have the effect of narrowing the ranges of applicability of the model. In general, the peeling and ballooning threshold depends on many different parameters, which make them difficult to parameterize. It is worthwhile to carry out an MHD stability analysis for a range of plasma parameters which are anticipated in the transport simulations, in order to derive an expression for the peeling-ballooning threshold as function of

these parameters. This parametric expression can be used in transport simulations. This approach is described in the next section of this paper in details.

III Peeling-ballooning stability analysis

Two reference case, which are based on two DIII-D discharges with different triangularity are considered further in this paper. Plasmas with high triangularity, $\delta = 0.6$, and low triangularity, $\delta = 0.2$, are considered. Other plasma parameters are held fixed in the reference cases: the minor radius $a = 0.63$ m; major radius $R = 1.69$ m; toroidal magnetic field $B_T = 2.0$ T; plasma current $I = 1.54$ MA; elongation $\kappa = 1.78$; central plasma density $n_e(0) = 4.7 \times 10^{19} \text{ m}^{-3}$; and central ion and electron temperatures $T_{e,i} = 4$ keV. The TOQ equilibrium code [18] is used to generate a set of equilibria that covers the range of transport simulations for the plasma parameters given above. As long as the plasma geometry, toroidal magnetic field, and total plasma current are fixed in the transport simulations, ELMs are controlled by only the pressure gradient and bootstrap current. The bootstrap current is computed in the TOQ code with the Sauter formula [30]

$$\langle j_{\parallel} B \rangle = \sigma_{\text{neo}} \langle E_{\parallel} B \rangle - I(\psi) p_e \left[\mathcal{L}_{31} \frac{p}{p_e} \frac{\partial \ln p}{\partial \psi} + \mathcal{L}_{32} \frac{\partial \ln T_e}{\partial \psi} + \mathcal{L}_{34} \lambda \frac{\partial \ln T_i}{\partial \psi} \right], \quad (10)$$

where σ_{neo} is the neoclassical resistivity, $I(\psi) = RB_{\phi}$, ψ is the normalized poloidal flux, and \mathcal{L}_{31} , \mathcal{L}_{32} , \mathcal{L}_{34} and λ are the bootstrap coefficients, which depend on the electron and ion collisionalities ν_{e*} and ν_{i*} , and on the trapped fraction f_t . The bootstrap current responds to changes in the plasma density and temperature in almost the same way as the normalized pressure gradient does. In order to find a peeling-ballooning stability threshold, it is convenient to use an additional control parameter, C_{boot} , for the bootstrap current in the DCON code:

$$\hat{j}_{\parallel} = C_{\text{boot}} j_{\parallel}. \quad (11)$$

The density and temperature profiles are defined with the following polynomial dependencies:

$$\begin{aligned} n_e(\psi) &= n_{\text{sep}} + a_{n0} \left[0.762 - \tanh \left(2 \frac{\psi - \psi_{\text{mid}}}{\Delta} \right) \right] \\ &\quad + a_{n1} H \left(1 - \frac{\psi}{\psi_{\text{ped}}} \right) \left[1 - \left(\frac{\psi}{\psi_{\text{ped}}} \right)^{\alpha_{n1}} \right]^{\alpha_{n2}}, \\ T_e(\psi) &= T_{\text{sep}} + a_{T0} \left[0.762 - \tanh \left(2 \frac{\psi - \psi_{\text{mid}}}{\Delta} \right) \right] \\ &\quad + a_{T1} H \left(1 - \frac{\psi}{\psi_{\text{ped}}} \right) \left[1 - \left(\frac{\psi}{\psi_{\text{ped}}} \right)^{\alpha_{T1}} \right]^{\alpha_{T2}}, \end{aligned} \quad (12)$$

where Δ is the pedestal width, H is the Heaviside step function, n_{sep} and T_{sep} are the electron density and temperature at separatrix respectively, $\psi_{\text{ped}} = 1 - \Delta$, and $\psi_{\text{mid}} = 1 - \Delta/2$. The constants a_{n0} , a_{n1} , a_{T0} and a_{T1} are computed in TOQ to satisfy the values of the plasma density and temperature at the top of the pedestal

and plasma center. The parameters α_{n1} , α_{n2} , α_{T1} , and α_{T2} control the shape of the electron density and temperature profiles in the plasma core. The profiles given by Eq. (12) reproduce the experimentally measured profiles [31] and were used in the peeling-ballooning ideal MHD stability analysis by Snyder *et al.* [28, 32]. The parameters that specify the profiles in the plasma core are kept the same for all scans: $\alpha_{n1} = \alpha_{n2} = \alpha_{T1} = 1.1$ and $\alpha_{T2} = 2$. Also, the shape of the electron density profile is kept unchanged in all scans; the electron density at the top of the pedestal is set to satisfy the dependence $n_{\text{ped}} = 0.71 \langle n_e \rangle$, which is observed in experiments [33]. In the density scan, the entire density profile is scaled as

$$\hat{n}_e(\psi) = C_{\text{dens}} n_e(\psi), \tag{13}$$

where C_{dens} is the control parameter in the TOQ code. In the temperature scan, the central temperature is kept fixed, while the pedestal temperature is changed (see Fig. 3). Both the bootstrap current and pressure gradient are changed in the density and temperature scans. The density scan provides more control of the bootstrap current, while the temperature scan provides more control of the normalized pressure gradient, α , which is defined in this study as

$$\alpha = -\frac{\mu_0}{2\pi^2} \frac{\partial p}{\partial \psi} \frac{\partial V}{\partial \psi} \left(\frac{V}{2\pi^2 R} \right)^{1/2}, \tag{14}$$

where V is the plasma volume and ψ is the poloidal flux.

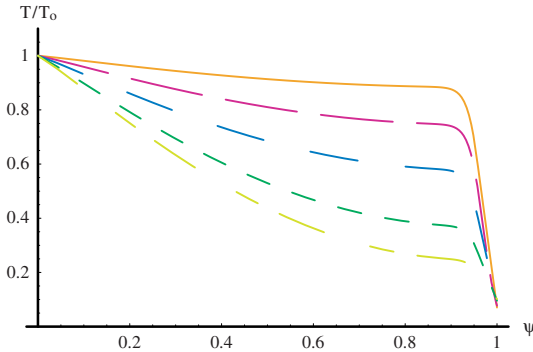


Fig. 3. Temperature profiles that are used in the TOQ code to generate a set of equilibria for analysis with the ideal MHD stability codes. The central temperature is fixed and the temperature at the top of the pedestal is changed.

In the reference equilibrium case, the central temperature is set to 4 keV and the central electron density is set to $4.7 \times 10^{19} \text{ m}^{-3}$. About 120 equilibria are generated for the high triangularity case and about 75 equilibria are generated for the low triangularity case by changing the TOQ parameters T_{ped} in the range from 250 keV to 3250 keV, C_{boot} in the range from 0.3 to 2.2, and C_{den} in the range from 0.5 to 3. These equilibria are used in the BALOO, DCON, and ELITE codes to validate the peeling-ballooning stability criteria in the limits of different toroidal mode numbers. The BALOO code [18] is an infinite mode number ballooning stability code developed at General Atomics. The ideal MHD DCON code is suitable for the stability analysis of low toroidal number ballooning and peeling modes, and the ELITE code works well for the analysis of intermediate and high mode numbers.

Since these codes are complementary, they can be used together to compute the stability criteria. The BALOO and DCON codes are called routinely from the same script that is used for the equilibrium generated by the TOQ code. The stability of low toroidal mode numbers up to $n = 7$ are analyzed with the DCON code. In addition, the DCON code has a criteria to check the stability of infinite n modes. That allows the results of DCON and BALOO to be cross-verified. The ELITE code is called for several questionable equilibria that are close to the peeling-ballooning stability threshold.

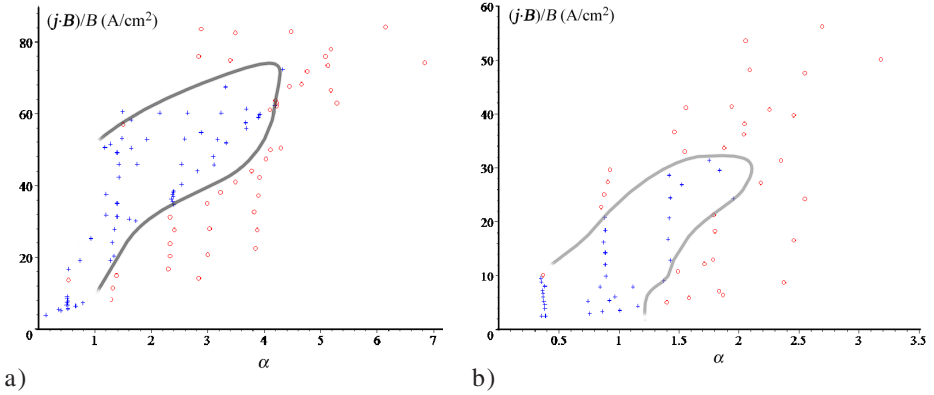


Fig. 4. ELM stability diagrams for discharges with (a) high ($\delta = 0.6$) and (b) low ($\delta = 0.2$) triangularity. Solid curve separates stable and unstable regions. The ‘+’ symbol on the diagrams corresponds to the cases that are tested with the MHD stability codes appear to be stable; the ‘o’ symbol on the diagram correspond to the cases that appear to be unstable.

The results of the stability analysis for high ($\delta = 0.6$) and low ($\delta = 0.2$) triangularity discharges are shown in Fig. 4. The solid curves in Fig. 4 separate the stable and unstable regions. The ‘+’ symbols mark stable regions of parameter space while the ‘o’ symbols mark unstable regions. The high triangularity discharge has a larger stable region than the low triangularity discharge, which is consistent with experimental results and other MHD stability analysis [32]. In particular, the higher triangularity discharges have a larger second stability region, which is also consistent with the conclusion that higher triangularity discharges can more easily access the second ballooning stability region of parameter space [3]. The peeling-ballooning threshold shown in Fig. 4 is parameterized using fifth order polynomials:

$$j_{\parallel}^{\text{stab}} = \sum_{i=0}^6 b_i \alpha^i, \quad (15)$$

where b_i are the parameterization coefficients. Each peeling-ballooning threshold is parameterized using two polynomials: one for the higher boundary (peeling threshold) and the other for the lower boundary (ballooning threshold). The polynomials for the peeling-ballooning threshold are implemented in the ASTRA transport code and used as the criteria to trigger ELM crashes in the transport simulations.

IV Results of integrated transport simulations

A reference scenario for ASTRA simulations is based on typical DIII-D geometry, using the parameters given at the beginning of previous section. In addition, the electron, ion, and impurity density profiles, toroidal rotation velocity, Z_{eff} , the current density driven by the neutral beam injection (NBI) heating, and the auxiliary heating power deposited to electrons and ions, which are obtained from an analysis simulation of experimental data, are prescribed and fixed in form. The experimental radial profile of the total current density is used as an initial condition for the magnetic diffusion equation, which is solved in the ASTRA code. The ASTRA code does not use the equilibria computed with the TOQ code described in the previous section of the paper; instead, the ESC equilibrium module is called to follow the dynamically evolving equilibrium in the ASTRA code.

In the reference scenario, the NBI auxiliary heating power deposited to electrons and ions in the simulation is increased from 1 MW to approximately 6 MW at 0.06 s, as shown in Fig. 5. In the ASTRA simulation, the electron and ion temperatures are observed to increase after the heating power increases, and the transition from L- to H-mode is observed at about 0.07 s. An H-mode pedestal is formed at this time in both electron and ion temperature profiles. For both the lower and

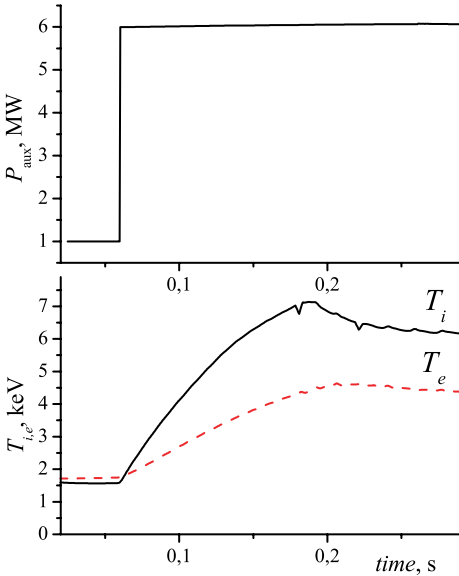


Fig. 5. The NBI heating power absorbed by the ions and electrons as a function of time is shown in the top panel. The electron and ion temperatures from Astra simulations are plotted as a function of time at the plasma center in the bottom panel.

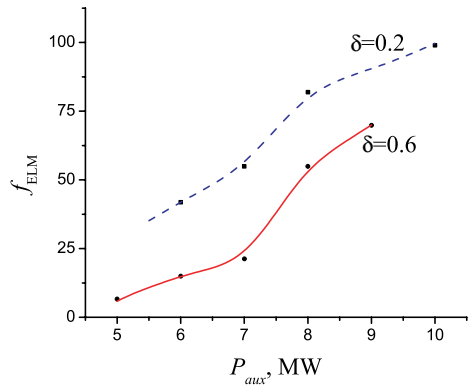


Fig. 6. The frequency of ELM crashes as function of the auxiliary heating power for discharges with low ($\delta = 0.2$) and high ($\delta = 0.6$) triangularities.

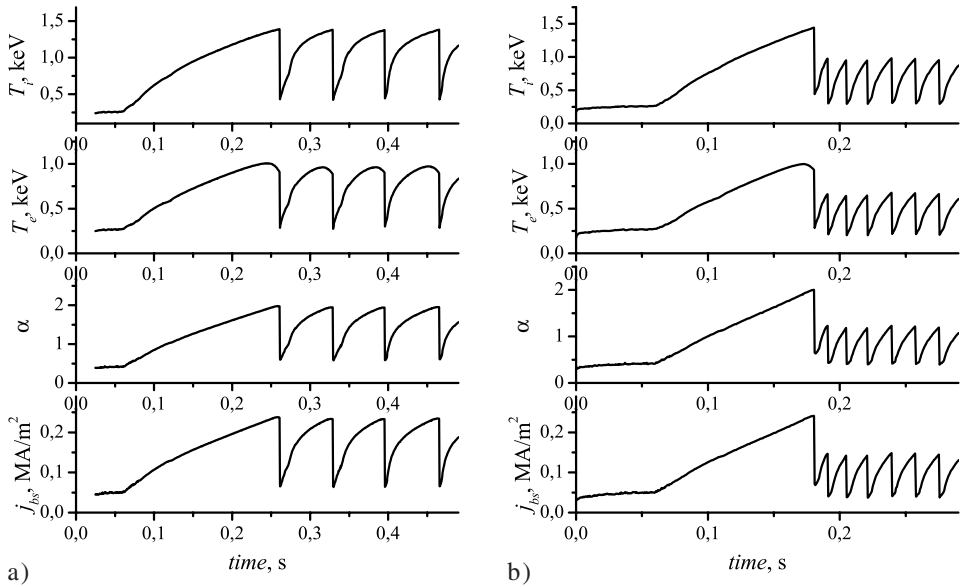


Fig. 7. Time evolution of electron and ion temperatures, normalized pressure gradient, and bootstrap current at 95% of the minor radius for the cases of a) lower (6 MW) and b) higher (8 MW) total auxiliary heating power.

higher triangularity discharges, the auxiliary heating power is varied from 3.5 MW to 7.0 MW in a series of simulations. The ELM frequencies as a function of auxiliary heating power for discharges with higher and lower triangularities are shown in Fig. 6. It can be seen that the ELM frequency increases with the heating power in the simulations, which is consistent with experimental observations in H-mode plasmas with type I ELMs.

In Ref. [5], two possible scenarios were discussed. In the first scenario, ELM crashes that are triggered by the ballooning instability in the first ballooning stability limit. In the second scenario, an ELM crash triggered by a ballooning instability in the first ballooning stability limit is followed by a series of frequent ELM crashes caused by the peeling instability. In the current study, a complete peeling-ballooning threshold is implemented and additional scenario is observed. For the higher triangularity discharge and higher auxiliary heating powers, a single ELM crash triggered by a ballooning instability in the first ballooning stability limit can be followed by series of more frequent ELM crashes triggered by a ballooning instability in the first ballooning stability limit (compare Figs. 7a and b). In general, access to the second stability region results in edge pressure gradients that reach higher levels. Because of this, the ELM crashes triggered by a ballooning instability in the first stability limit are less frequent than the ELM crashes triggered by a ballooning instability in the second stability limit. The change of the slope of the ELM frequency as a function of heating power, shown in Fig. 6, can

be explained by the different scenarios that are followed for low and high auxiliary heating discharges. In the ASTRA simulations, the discharges with low auxiliary heating (below 7 MW) have ELM crashes that are triggered by a ballooning instability in the second stability limit, while the discharges with high heating power (above 7 MW) are triggered by a ballooning instability in the first stability limit.

V Summary

An improved model is introduced for H-mode pedestal and ELMs [5]. A parameterized peeling-ballooning stability criterion is implemented in the model, based on detailed MHD analyses with the BALOO, DCON, and ELITE codes. Two different scenarios for ELM crashes in DIII-D discharges are shown. For the scenario with lower auxiliary heating power, ELMs are mostly caused by the ballooning instability in the second stability limit. For the scenario with higher auxiliary heating power (above 7 MW), ELMs might be caused by the ballooning instability in the first stability limit. Such ELM crashes are much less violent and more frequent. In general, the frequency of ELMs increases with the auxiliary heating power (as shown in Fig. 6), which is consistent with the experimental observations. The frequency of ELMs also depends on the plasma shaping. In particular, the dependence on the triangularity is studied in this paper. It is found that higher triangularity discharges have a larger stability region than lower triangularity discharges (compare Figs. 4a and b). This observation is consistent with other MHD stability analysis [32] and the conclusion that higher triangularity discharges can more easily access the second ballooning stability limit region of parameter space [3]. As result, ELMs in lower triangularity discharges are much more frequent than ELMs in higher triangularity discharges (as shown in Fig. 6).

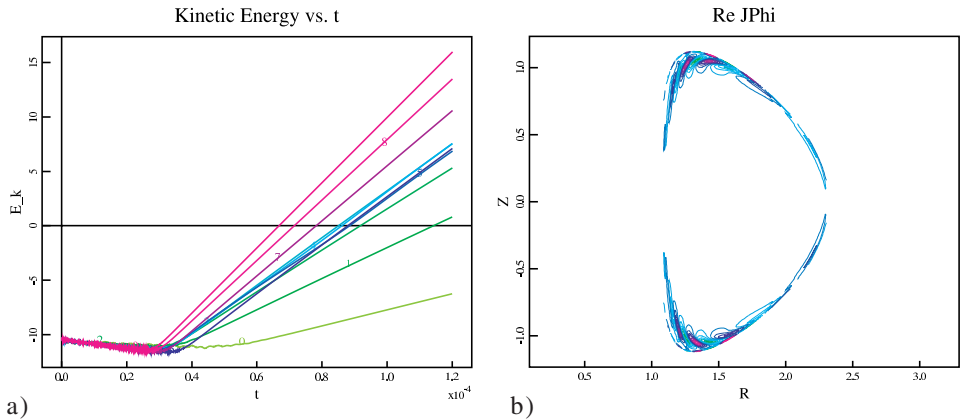


Fig. 8. Results of the resistive MHD NIMROD code simulations for the first 10 toroidal mode numbers: a) logarithm of the kinetic energy for different mode numbers; b) contour plot of the eigen-functions.

In conclusion, it is clear that additional MHD stability studies are required. In this paper, ideal MHD stability codes are used, while resistivity and two-fluid effects are expected to be important. A preliminary study with the resistive MHD NIMROD [34] code is under way. Some of the results of these simulations are shown in Fig. 8. The equilibrium selected for the NIMROD simulation corresponds to a stable case that is close to the nose of the stability diagram on Fig. 4a. It is shown in Fig. 8a that modes with low toroidal mode numbers ($n \leq 10$) are linearly unstable. The NIMROD code uses exactly the same equilibrium generated with the TOQ code. At the same time, the equilibrium is not extended into the vacuum region in the NIMROD code. (In the DCON code, the extension of the equilibrium into the vacuum region is carried out using the supplementary code VACUUM [35]). In order to be consistent, an equilibrium with the settings that eliminate the vacuum region has been analyzed with the DCON code. The DCON results show that peeling mode is unstable for the low toroidal mode numbers shown in this case, which might be the case that is observed with the NIMROD code. The eigen-functions shown in Fig. 4b are very localized close to separatrix, which might indicate the signature of a peeling instability. In order to verify the results obtained with the MHD ideal stability code, a robust vacuum code should be used together with the NIMROD code which will be done in future studies.

The authors thank Dr. G. Pereverzev for installation and support of the ASTRA code, Dr. L. E. Zakharov for installation and help with the ESC equilibrium module.

References

- [1] G. Pacher, H. Pacher, G. Janeschitz et al.: Plasma Phys. Control. Fusion **46** (2004) A257.
- [2] R. Schneider, X. Bonin, N. McTaggart, A. Runov, M. Borchardt et al.: *Comprehensive suite of codes for plasma-edge modeling*, to appear in Comp. Phys. Commun. (2004).
- [3] T. Onjun, A. H. Kritz, G. Bateman et al.: Phys. Plasmas **11** (2004) 3006.
- [4] J.-S. Lönnroth, V. V. Parail, A. Dnestrovskij et al.: Plasma Phys. Control. Fusion **46** (2004) 1197.
- [5] A. Y. Pankin, I. Voitsekhovitch, G. Bateman et al.: Plasma Phys. Control. Fusion **46** (2004).
- [6] O. V. Zolotukhin, Y. Igitkhanov, G. Janeschitz et al.: in *28th EPS Conf. on Contr. Fusion and Plasma Phys., Funchal, Portugal, June 2001*, ECA, Vol. **46C**, 2001, p. 677.
- [7] S. Hamaguchi and W. Horton: Phys. Fluids B **4** (1992) 319.
- [8] T.S. Hahm and K.H. Burrell: Phys. Plasmas **2** (1995) 1648.
- [9] K.H. Burrell: Phys. Plasmas **4** (1997) 1499.
- [10] G.M. Staebler, R.E. Waltz, and J.C. Wiley: Nuclear Fusion **37** (1997) 287.
- [11] T.S. Hahm and P.H. Diamond: Phys. Fluids **30** (1987) 133.
- [12] A.M. Dimits, B.I. Cohen, W.M. Nevins, and D.E. Shumaker: Nucl. Fusion **40** (2001) 1725.

- [13] G. Bateman, A.H.K.J. Kinsey, A. Pankin et al.: in *Proc. of the Int. Sherwood Fusion Theory Meeting, Corpus Cristi, TX, April 2003*, (Editor?), Publisher?, City?, 2003, Page?.
- [14] M. Sugihara, Y. Igitkhanov, G. Janeschitz et al.: *Nucl. Fusion* **40** (2000) 1743.
- [15] G. Bateman, A.H. Kritz, J.E. Kinsey, A.J. Redd, and J. Weiland: *Phys. Plasmas* **5** (1998) 1793.
- [16] J.W. Connor: *Plasma Phys. Control. Fusion* **40** (1998) 531.
- [17] L.L. Lao: *Plasma Phys. Control. Fusion* **42** (2000) A51.
- [18] R.L. Miller and J.W. VanDam: *Nucl. Fusion* **28** (1987) 2101.
- [19] A.H. Glasser and M.S. Chance: *Bull. Am. Phys. Soc.* **42** (1997) 1848.
- [20] H.R. Wilson, P.B. Snyder, R.L. Miller, and G.T.A. Huysmans: *Phys. Plasmas* **9** (2002) ■.
- [21] G. Pereverzev and P.N. Yushmanov: *ASTRA Automated System for TRansport Analysis in a Tokamak*, Tech. Rep. IPP 5/98, Max-Planck Institut für Plasmaphysik, 2002.
- [22] J. Weiland and A. Hirose: *Nucl. Fusion* **32** (1992) 151.
- [23] P.N. Guzdar, J.F. Drake, D. McCarthy, and A.B. Hassam: *Phys. Fluids B* **5** (1993) 3712.
- [24] W. Horton, P. Zhu, G.T. Hoang et al.: *Phys. Plasmas* **7** (2000) 1494.
- [25] W.A. Houlberg, K.C. Shaing, S.P. Hirshman, and M.C. Zarnstorff: *Phys. Plasmas* **4** (1997) 3230.
- [26] P.N. Guzdar, R.G. Kleva, A. Das, and P.K. Kaw: *Phys. Rev. Lett.* **87** (2001) 015001.
- [27] Y.B. Kim, P.H. Diamond, and R.J. Groebner: *Phys. Fluids B* **3** (1991) 2050.
- [28] P.B. Snyder, H.R. Wilson, J.R. Ferron et al.: *Phys. Plasmas* **9** (2002) 2037.
- [29] H. Wilson, J.W. Connor, A.R. Field et al.: *Nucl. Fusion* **40** (2000) 713.
- [30] O. Sauter, C. Angioni, and Y.R. Lin-Liu: *Phys. Plasmas* **6** (1999) 2834.
- [31] T.H. Osborne et al.: *Plasma Phys. Control. Fusion* **42** (2000) ■.
- [32] P.B. Snyder, H.R. Wilson et al.: *Nucl. Fusion* **44** (2004) 320.
- [33] T. Onjun, G. Bateman, A.H. Kritz, and G. Hammett: *Phys. Plasmas* **9** (2002) 5018.
- [34] C.R. Sovinec, D.C. Barnes, T.A. Gianakon et al.: *J. Comp. Phys.* (2004).
- [35] M.S. Chance: *Phys. Plasma* **4** (1997) 2161.